

Title here

Author One,^a Author Two,^a Author Three,^b Author Four,^a Author Five,^c Author Six,^d Author
Seven,^d and Author Eight^{a,d}

^a *First Affiliation*

^b *Second Affiliation*

^c *Third Affiliation*

^d *Fourth Affiliation*

Author Five’s current affiliation: NCAR, Boulder, Colorado

9 ABSTRACT: Enter the text of your abstract here. This is a sample American Meteorological
10 Society (AMS) L^AT_EX template. This document provides authors with instructions on the use of the
11 AMS L^AT_EX template. Authors should refer to the file amspaper.tex to review the actual L^AT_EX code
12 used to create this document. The template.tex file should be modified by authors for their own
13 manuscript.

14 Enter significance statement here, no more than 120 words. See www.ametsoc.org/index.cfm/ams/publications/author-information/significance-statements/ for details.

15 Enter BAMS capsule here, no more than 30 words. See www.ametsoc.org/index.cfm/ams/publications/author-information/formatting-and-manuscript-components/\#capsule for details

19 1. Introduction

20 It has now become our basic knowledge that the extratropical atmosphere is driven strongly by the
21 horizontal potential temperature gradient that arises from the differential solar heating (e.g., Lorenz
22 1955). The horizontal gradient in the potential temperature, often referred to as baroclinicity, is a
23 measure of upper-level wind steering via thermal wind and a measure of baroclinic instability in
24 the atmosphere. Baroclinicity in the lower atmosphere in classic theories of atmospheric stability
25 is measured by a combination of the static stability and horizontal temperature gradient, the latter
26 of which is equivalent to vertical shear in the horizontal wind through the thermal wind balance
27 (Charney 1947; Eady 1949). In its original form, the Eady's maximum growth rate for baroclinic
28 instability B_{GRMax} is defined by $B_{GRMax} = 0.31(|f|/N)(\partial U/\partial_z)$ in a zonally homogeneous steady
29 mean state, where U is the mean zonal flow, f is the Coriolis parameter, and N is the Brunt–Väisälä
30 frequency. Charney's formula is slightly different from the Eady's, but still incorporates the same
31 effects (Table 1).

35 Lindzen and Farrell (1980) first applied the Eady's parameter to atmospheric data to successfully
36 estimate the maximum growth rate of baroclinic instability in the troposphere. Hoskins and Valdes
37 (1990) used its localized version (i.e., U , N , and f are all local Eulerian mean values) as the
38 central parameter in their study of the Northern Hemispheric storm tracks. This local version, or
39 its simplified version, has been used successfully as an indicator of baroclinic wave generation in
40 diagnostic studies of stormtracks in recent years as well (Nakamura and Sampe 2002; Nakamura
41 and Shimpo 2004; Nakamura et al. 2004). In our study, the North Atlantic part of which was
42 reported in Nakamura and Yamane (2009, hereafter Part I), we define the near-surface baroclinic
43 vector, $\mathbf{B} = B^x\mathbf{i} + B^y\mathbf{j}$, where $B^x = -(g/\theta N)(\partial\theta/\partial y)$ and $B^y = (g/\theta N)(\partial\theta/\partial x)$ with θ being the
44 monthly-mean potential temperature at 2 m above the surface, and use it as the central quantity
45 of the diagnoses. Unless stated otherwise, “anomalies” refer to deviations from the climatology

Month	EOF1	Split	EOF2	Split	EOF3	EOF4
Jan	29	NG	24	GD	10	5
Feb	39	GD	20	GD	7	6
Mar	31	GD	14	NG	10	6
Apr	23	GD	14	NG	10	7
May	19	GD	12	NG	10	7
Jun	19	GD	12	NG	10	9
Jul	18	NG	13	NG	9	7
Aug	18	NG	13	NG	11	9
Sep	17	NG	13	NG	10	8
Oct	16	NG	13	GD	8	7
Nov	19	NG	16	NG	11	8
Dec	33	GD	18	GD	10	6

TABLE 1. Percentage of variance explained by the first four EOFs for the North Pacific Bx. The degree of separation between EOF1 and EOF2 and EOF2 and EOF3, based on the North et al. (1982) criterion, is indicated by good (GD) and not good or marginal (NG).

hereafter. Though its meridional component does not appear in any classic theory of baroclinic instability, a theory that does incorporate the effect of B^y shows its important role in enhancing baroclinic wave generation locally to the east of the mean trough (Niehaus 1980). In the North Atlantic storm track region, we indeed found that the substantial zonal gradient in the surface temperature in and around the Labrador Sea plays a major role in the large-scale atmospheric state.

2. The sea surface temperature

The sea surface temperature (SST) is an important factor in determining \mathbf{B} in the storm-track regions (e.g., Hoskins and Valdes 1990; Nakamura et al. 2004; Part I). SST anomalies (SSTAs) around an oceanic front along the Gulf Stream (GS), Kuroshio Extension (KE), or Oyashio Extension (OE) can have a profound impact on \mathbf{B} along the storm tracks.

a. A subtle point

A subtle but important point that has to be considered carefully in this regard is the spatial scale and the location of SSTAs with respect to the climatology, since it is the anomalous surface temperature gradient whose structure has a spatial scale of the atmospheric Rossby deformation radius that can exert significant influence on the large-scale atmospheric flow.

1) CHANGES IN THE TEMPERATURE

The high sensitivity of **B** to changes in the temperature contrast across the front and changes in the width of the front, and the uncertainty in the impact of SSTAs of small spatial scales on **B** make it difficult to assess the effective **B** anomalies that are attributable to the SSTAs from the available data. Moreover, it is uncertain exactly how the SSTAs in the presence or absence of the land surface temperature anomalies may or may not produce **B** anomalies that are significant to the atmosphere.

(i) Complicating factor The complicating factor introduced by the land surface must be taken into account when studying potential roles of extratropical SSTAs in the extratropical atmospheric anomalies. Lau (1988) investigated patterns of anomalous storm track activity and associated low-frequency flow anomalies by computing empirical orthogonal functions (EOFs) for high-frequency 500-hPa geopotential height for the Northern Hemisphere winters. He found that both North Atlantic and North Pacific storm tracks have a pattern of meridional shift and a pattern of increased or decreased eddy activity in the first two EOFs. He also found that these changes in the storm tracks have symbiotic relationships with the background flows and have substantial impacts on the mean flow. Part I approached the issue of the stormtrack and low-frequency flow variability in connection with SSTAs in the extratropics, focusing on **B** as the key parameter of diagnoses, and found similar patterns of variability in the eddy activity and low-frequency flow in the North Atlantic basin. Much of this variability was connected to SSTAs in the vicinity of the Gulf Stream in cold months (Part I). Since the winter North Pacific basin has a storm track and mean flow that appear to be related to the oceanic fronts, Kuroshio–Oyashio Extensions (KOE) in this case, in a manner essentially the same as those in the North Atlantic basin related to the GS, we have attempted to find similar results for the North Pacific basin. In this regard, we have chosen not to project our results onto the major mode of variability in the extratropical North Pacific basin, the North Pacific decadal variability (PDV), so that our presentation and discussion are mostly confined to the wave–mean flow dynamics of monthly time scale or shorter.

Our approach to the search for a link between anomalies in the KOE and the overlying atmosphere is as follows: (i) identify dominant patterns in anomalous **B** in the storm track for each calendar-month and identify years in which the anomaly fits the pattern well, (ii) composite anomalies in the monthly-mean circulation and high-frequency transients in the atmosphere to obtain a typical

atmospheric state that accompanies the patterns of anomalous \mathbf{B} , (iii) composite SSTA to obtain a typical oceanic state that accompanies and precedes the patterns of anomalous \mathbf{B} , and (iv) composite anomalous net surface heat flux that accompanies and precedes the pattern of anomalous \mathbf{B} . With this approach, we obtain typical pictures of anomalous states in the atmosphere and oceans with anomalous \mathbf{B} as their connecting interface. Section 2 describes the data and procedure to compute \mathbf{B} . Section 3 describes the climatology and variance of \mathbf{B} . Dominant patterns of \mathbf{B} are shown in section 4, followed by composited anomalies in various atmospheric fields and SST in section 5. Finally, we present our discussion on the results, examining a potential cause–effect relationship between anomalies in the SST and atmosphere in section 6.

Figure 1 shows the climatology of B_x , U^{200} , $\overline{V'\theta'}^{850}$, $\overline{V'\theta'}^{200}$, MR^{850} , U^{1000} , SST, and F_h for February and August as examples of the reference state in the winter and summer. The numeric superscript indicates the pressure level in hPa. The seasonal mean is visibly more diffused in structure, particularly for B_x , than those shown in Fig.~1. There are no surprises in the overall picture of B_x . The regions of large land–sea temperature contrast and the oceanic fronts show very large B_x in cold months. The position of B_x maximum in the storm track region is found along the KOE region throughout the year. The zonally elongated band of large B_x in the storm track is generally wider in cold months than in warm months. In fact, large B_x values that presumably accompany the Kuroshio and its extension in the cold months vanish in the summer (Figs. 1a,b). The seasonal variation in the B_x values in the storm track basically follows that of the north–south differential heating—largest in the winter and smallest in the summer. As reported by Nakamura et al. (2004), the U^{200} maximum is displaced southward from the B_x maximum visibly in winter months (Fig. 2a), although U^{200} is generally large over the area of large B_x in the core of the storm track. The southward displacement of the U^{200} maximum from the B_x maximum in the storm track is less pronounced or even reversed in warmer months (Fig. 2b). We note that the structure of the climatological B_x generally reflects those of $(\partial\theta^{2m}/\partial y)$ with some exceptions where the surface slope contributes significantly to B_x in isolated areas over the land, most notably around the Himalayas.

The position and structure of the storm track as indicated by $\overline{V'\theta'}^{850}$ and $\overline{V'V'}^{200}$ are, at least for the winter, essentially the same as those reported in earlier studies on the storm tracks (e.g., Chang et al. 2002). The maxima in $\overline{V'\theta'}^{850}$ and $\overline{V'V'}^{200}$ are located in the band of large B_x .

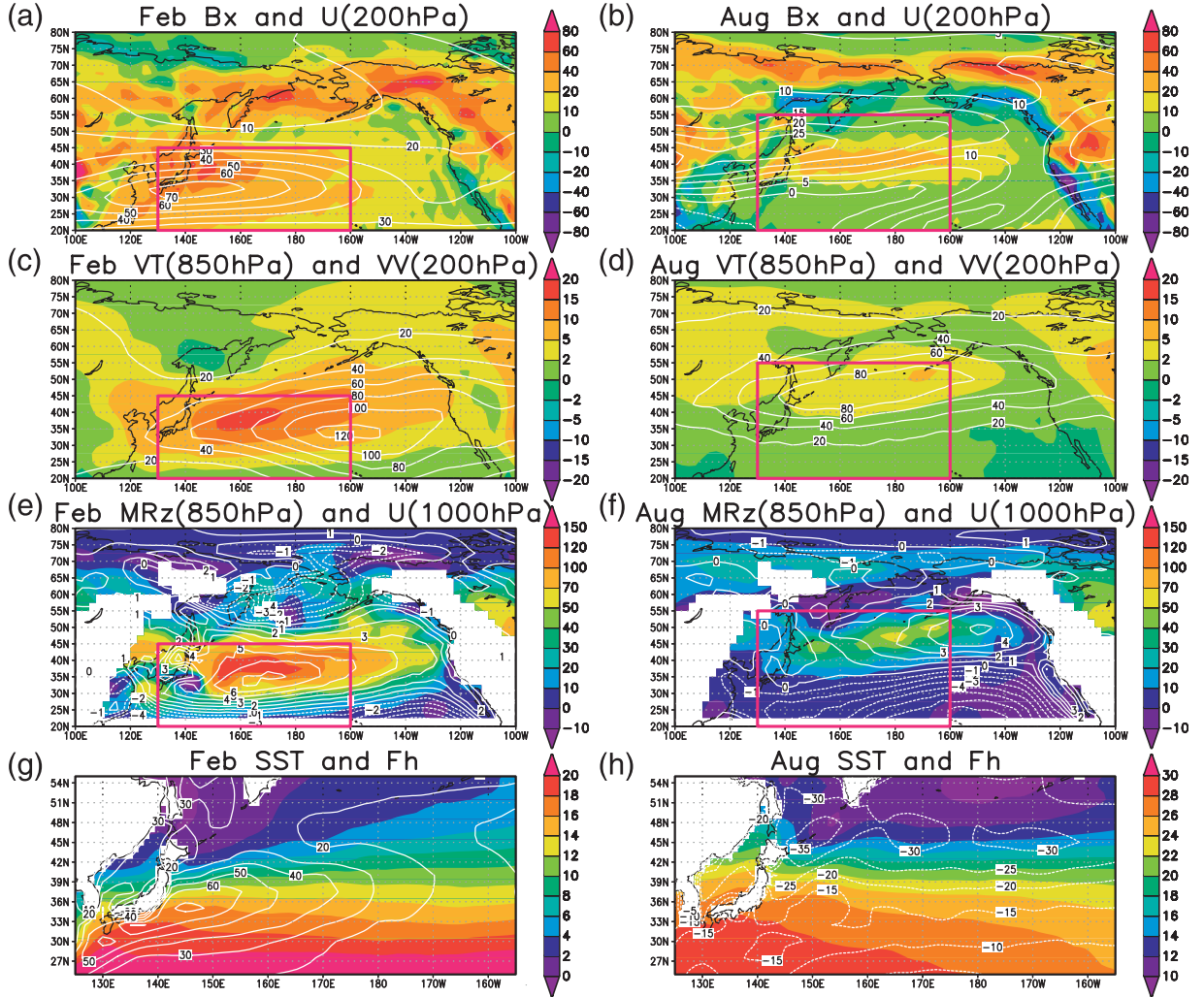


FIG. 1. Climatology of $Bx(10^{-6}s^{-1}, \text{color})$ and $U^{200}(\text{m s}^{-1}, \text{contours})$ for (a) February and (b) August; $\overline{V'\theta'}^{850}$ ($\text{K m s}^{-1}, \text{color})$ and $\overline{V'V'}^{200}$ ($\text{m}^2 \text{s}^{-1}, \text{contours})$ for (c) February and (d) August; MR^{z850} ($10^{-3} \text{m}^2 \text{s}^{-2}, \text{color})$ and U^{1000} ($\text{m s}^{-1}, \text{contours})$ for (e) February and (f) August; and SST ($\text{K}, \text{color})$ and $F_h [10^5 \text{J m}^{-2} (6 \text{h})^{-1}]$ for (g) February and (h) August. Red rectangles indicate the domain of EOF calculations.

3. Data and calculation procedures

The data used to calculate \mathbf{B} are the monthly-mean temperature at 2 m above the surface (T^{2m}) and temperature at pressure levels available from the 40-yr European Centre for Medium-Range Weather Forecasts (ECMWF) Re-Analysis (ERA-40; Uppala et al. 2005). We chose the ERA-40 T^{2m} data rather than the National Centers for Environmental Prediction–National Center for Atmospheric Research (NCEP–NCAR) reanalysis products for its explicit inclusion of the observed

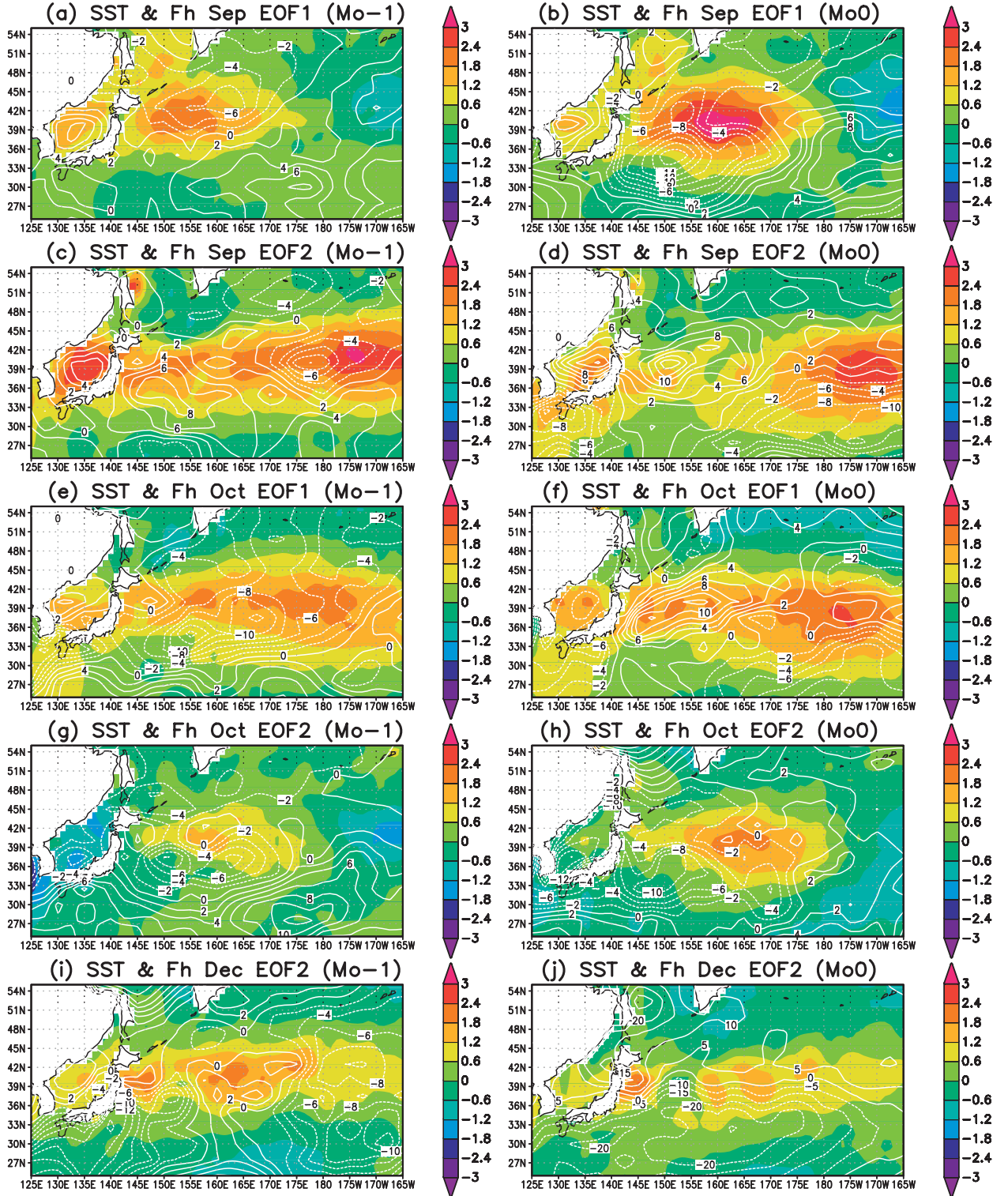


FIG. 2. As in Fig. 10, but for (a),(b) September EOF1; (c),(d) September EOF2; (e),(f) October EOF1; (g),(h)

October EOF2; and (i),(j) December EOF2.

133 near-surface temperature in producing the T^{2m} data. The monthly-mean surface pressure data from
 134 the NCEP–NCAR reanalyses (Kalnay et al. 1996) were used to determine the pressure levels to
 135 be used for **B** calculation, and to calculate θ at 2 m above the surface from T^{2m} . We used the
 136 NCEP–NCAR surface pressure data for convenience, since we had already compiled the dataset for
 137 calculating transient eddy fluxes to be mentioned later and the ERA-40 surface pressure data are
 138 not readily available. We later compared the NCEP–NCAR monthly-mean sea level pressure with
 139 that of ERA-40, and found the difference between the two products to be immaterial for the purpose
 140 of the current study. We also used ERA-40 monthly-mean horizontal wind and geopotential height
 141 at pressure levels, net surface heat flux, Fh (the sum of latent heat flux, sensible heat flux, solar
 142 radiation, and the thermal radiation), and Hadley Centre sea surface temperature data (Rayner et
 143 al. 2003) to compile anomaly composites accompanying anomalous patterns in **B**. In addition, we
 144 used 6-hourly temperature and wind data from the NCEP–NCAR reanalyses to compute various
 145 eddy fields. The accuracy of the Fh data used here is, as true for other reanalyses surface heat flux
 146 products, may not be so high to produce reliable anomaly composites.

147 We computed **B** near the surface by calculating the horizontal gradient in θ^{2m} , using the centered
 148 finite differencing, and calculating N from the lowest three vertical pressure levels that are location
 149 dependent because of topography. Both $\nabla\theta^{2m}$ and N were calculated locally as in Hoskins and
 150 Valdes (1990) and Nakamura and Shimpo (2004). The entire 45 yr from September 1957 to August
 151 2002 were used for the Northern Hemisphere. To resolve the dominant modes in **B** arising from
 152 the land–sea temperature contrast, one may need much higher horizontal resolution in the data.
 153 The relatively coarse horizontal resolution of the data may artificially suppress the significance of
 154 the variability associated with the land–sea temperature contrast. One should keep this limitation in
 155 mind. The 6-hourly bandpassed (period of 2–7 days) eddy fields and ultra-low-frequency (period
 156 of 30 days and longer) background fields were computed from the NCEP–NCAR reanalyses, using
 157 simple time filters (Lau and Lau 1984) first. The filtered time series were then visually examined
 158 against the raw time series and, then, used to calculate the slowly evolving bandpassed meridional
 159 velocity variance ($\overline{V'V'}$), meridional temperature flux ($\overline{V'\theta'}$), and the three-dimensional transient
 160 wave activity flux defined on a zonally varying basic state by Plumb (1986). The wave activity
 161 flux consists of the zonal and meridional advective fluxes (MU and MV), the zonal and meridional
 162 radiative fluxes (MRx and MRy), and the radiative vertical flux (MRz). The flux is essentially

the Eliassen–Palm flux (Eliassen and Palm 1961) in a zonally inhomogeneous mean flow (Plumb 1986). The wave activity flux was calculated from February 1948 to November 2004 only for the extratropics poleward of 20° latitude. Also, it was calculated only from 850 to 30 hPa because of the double differentiation with respect to pressure required for the calculation. The flux of particular interest in this study is the vertical component. Here MR^z is defined by

$$MR^z = \frac{p f \cos \phi}{p^0 |\nabla h \bar{q}| (d\theta_0/dz)} \left(\frac{\partial \bar{q}}{\partial x} \overline{U'\theta'} + \frac{\partial \bar{q}}{\partial y} \overline{V'\theta'} \right),$$

where q is quasigeostrophic potential vorticity, p is the pressure, p^0 is the reference surface pressure set to 1000 hPa here, θ_0 is the area-weighted ultra-low-frequency hemispheric mean potential temperature at each height, u_9 is the bandpassed potential temperature, and z is the geopotential height. An overbar denotes an ultra-low frequency component and a prime denotes bandpassed component. The 6-hourly time series of wave fluxes was computed by using the time series of ultra-low-frequency fields as the basic-state and high-frequency fields as eddies. In short, the time series was calculated by changing the meaning of an overbar from the time mean state to an ultra-low-frequency state, and changing the meaning of a prime from a departure from the mean to a high-frequency state. The 6-hourly eddy time series was averaged over each month to produce monthly-mean time series. This dataset allows us to examine anomalous eddy fields accompanying anomalous \mathbf{B} in specific months. The climatology for the eddy fields was computed from 46 yr, January 1958 to December 2003. The calculation of the wave activity and its flux is described in detail by Nakamura et al. (2010).

4. Climatology and variance

The climatology and variance of B_x and B_y were computed for each calendar month and examined closely for their spatial and temporal structures. The monthly climatology, rather than the seasonal climatology, is used as the reference in our study, to avoid contamination of the diagnostic results arising from differences in the climatology between two successive months. Unlike in the North Atlantic basin reported in Part I, we found the impact of B_y variations on the large-scale atmospheric state in the North Pacific basin much weaker than that of B_x variations, presumably because of the more zonal orientation of the KOE in comparison to the Gulf Stream

189 and North Atlantic Current. In the following, thus, we focus our presentation on the climatology
190 and variations of Bx and their impact on the large-scale atmospheric state.

191 Sample citations: Becker and Schmitz (2003), Knutti et al. (2008), and (Meixner et al. 2002;
192 Kuji and Nakajima 2002; Emery et al. 1986).

We thank two anonymous reviewers for their comments, which helped to improve the manuscript.
Start data availability statement here.

5. Appendix Title

Appendix section head

Here is a sample appendix with an equation [see Eq. (1)]. Lorem ipsum dolor sit amet, consectetur adipiscing elit, sed do eiusmod tempor incididunt ut labore et dolore magna aliqua. Ut enim ad minim veniam, quis nostrud exercitation ullamco laboris nisi ut aliquip ex ea commodo consequat.

$$\frac{pf \cos \phi}{p^0 |\nabla h \bar{q}| (d\theta_0/dz)} \quad (1)$$

Lorem ipsum dolor sit amet, consectetur adipiscing elit, sed do eiusmod tempor incididunt ut labore et dolore magna aliqua. Ut enim ad minim veniam, quis nostrud exercitation ullamco laboris nisi ut aliquip ex ea commodo consequat. Duis aute irure dolor in reprehenderit in voluptate velit esse cillum dolore eu fugiat nulla pariatur. Excepteur sint occaecat cupidatat non proident, sunt in culpa qui officia deserunt mollit anim id est laborum.

Lorem ipsum dolor sit amet, consectetur adipiscing elit, sed do eiusmod tempor incididunt ut labore et dolore magna aliqua. Ut enim ad minim veniam, quis nostrud exercitation ullamco laboris nisi ut aliquip ex ea commodo consequat. Here is an example appendix figure (see Fig. 3).

6. Second Appendix Title

a. Sample appendix section head

Lorem ipsum dolor sit amet, consectetur adipiscing elit, sed do eiusmod tempor incididunt ut labore et dolore magna aliqua. Ut enim ad minim veniam, quis nostrud exercitation ullamco laboris nisi ut aliquip ex ea commodo consequat [see Eq. (2)]. Duis aute irure dolor in reprehenderit in voluptate velit esse cillum dolore eu fugiat nulla pariatur. Excepteur sint occaecat cupidatat non proident, sunt in culpa qui officia deserunt mollit anim id est laborum.

$$\left(\frac{\partial \bar{q}}{\partial x} \overline{U' \theta'} + \frac{\partial \bar{q}}{\partial y} \overline{V' \theta'} \right) \quad (2)$$

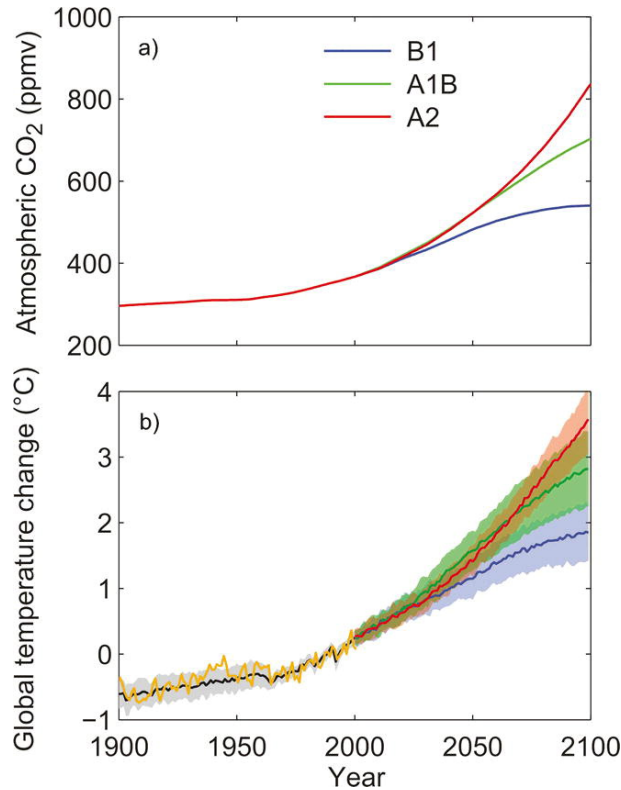


FIG. 3. Here is an appendix, single column figure caption.

216 Lorem ipsum dolor sit amet, consectetur adipiscing elit, sed do eiusmod tempor incididunt ut
 217 labore et dolore magna aliqua. Ut enim ad minim veniam, quis nostrud exercitation ullamco laboris
 218 nisi ut aliquip ex ea commodo consequat. Duis aute irure dolor in reprehenderit in voluptate velit
 219 esse cillum dolore eu fugiat nulla pariatur. Excepteur sint occaecat cupidatat non proident, sunt
 220 in culpa qui officia deserunt mollit anim id est laborum. Lorem ipsum dolor sit amet, consectetur
 221 adipiscing elit, sed do eiusmod tempor incididunt ut labore et dolore magna aliqua. Ut enim ad
 222 minim veniam, quis nostrud exercitation ullamco laboris nisi ut aliquip ex ea commodo consequat.
 223 Duis aute irure dolor in reprehenderit in voluptate velit esse cillum dolore eu fugiat nulla pariatur.
 224 Excepteur sint occaecat cupidatat non proident, sunt in culpa qui officia deserunt mollit anim id est
 225 laborum.

226 *b. Sample appendix section head*

227 Second appendix example. Here an example appendix table (see Table 2).

Month	Yr of positive phase
Jan	1961, 1969, 1978, 1979, 1988, 1990, 1992, 1994
Feb	1964, 1977, 1978, 1980, 1983, 1986, 1988, 2000, 2001
Mar	1970, 1973, 1979, 1980, 1984, 1988, 2000
Apr	1959, 1961, 1962, 1963, 1968, 1972, 1983, 2002
May	1971, 1984, 1993, 1996, 2000
Jun	1981, 1983, 1984, 1993, 1998
Jul	1961, 1972, 1973, 1978, 1994, 2000
Aug	1967, 1970, 1973, 1978, 1994, 1999
Sep	1975, 1977, 1988, 1989, 1994, 1998, 1999
Oct	1962, 1977, 1998, 1999, 2001
Nov	1985, 1986, 1987, 1988, 1991, 1998
Dec	1957, 1968, 1972, 1978, 1979, 1990

TABLE 2. Years selected for anomaly composites for the positive phase of B^x EOF1.

References

- Becker, E., and G. Schmitz, 2003: Climatological effects of orography and land–sea heating contrasts on the gravity wave–driven circulation of the mesosphere. *J. Atmos. Sci.*, **60**, 103–118, [https://doi.org/10.1175/1520-0469\(2003\)060<0103:CEOOAL>2.0.CO;2](https://doi.org/10.1175/1520-0469(2003)060<0103:CEOOAL>2.0.CO;2).
- Emery, W. J., A. C. Thomas, M. J. Collins, W. R. Crawford, and D. L. Mackas, 1986: An objective method for computing advective surface velocities from sequential infrared satellite images. *J. Geophys. Res.*, **91**, 12 865–12 878, <https://doi.org/10.1029/JC091iC11p12865>.
- Knutti, R., and Coauthors, 2008: A review of uncertainties in global temperature projections over the twenty-first century. *J. Climate*, **21**, 2651–2663, <https://doi.org/10.1175/2007JCLI2119.1>.
- Kuji, M., and T. Nakajima, 2002: Retrieval of cloud geometrical parameters using remote sensing data. *11th Conf. on Cloud Physics*, Ogden, UT, Amer. Meteor. Soc., JP1.7, <http://ams.confex.com/ams/pdfpapers/39550.pdf>.
- Meixner, T., L. A. Bastidas, H. V. Gupta, and R. C. Bales, 2002: Multicriteria parameter estimation for models of stream chemical composition. *Water Resour. Res.*, **38**, 1027, <https://doi.org/10.1029/2000WR000112>.